

Supporting Information

Why does Y6 with bulk charge photogeneration and bipolar charge transport properties still fail in non-heterojunction organic photovoltaics?

Yuhao Xie,^a Yu Cui,^a Dmitry Yu. Paraschuk,^b Wei Ma,^a and Han Yan^{*a}

^aState Key Laboratory for Mechanical Behavior of Materials; School of Materials Science and Engineering, Xi'an Jiaotong University, Xi'an 710049, P. R. China.

E-mail: mseyanhan@xjtu.edu.cn

^bFaculty of Physics, Lomonosov Moscow State University, Leninskie Gory 1/62, Moscow 119991, Russia

Table of Contents

Experimental Section	3
Materials	3
Instrument	3
Device fabrication	3
Calculation of J_{\max}	4
Cyclic voltammetry measurements	5
Impedance measurements	5
Space charge limited current (SCLC) characteristics	6
Calculation of $L_{\text{EX+CS}}$	7
DFT calculation	8
Fig. S1. Chemical structures of PM6, Y6 and N4	9
Fig. S2. Absorption comparison and EQE curves of BHJ devices	10
Fig. S3. J-V and EQE curves of Y6-based NHJ OSCs	10
Fig. S4. AFM images of pure Y6 and PM6:Y6 BHJ film	11
Fig. S5. Optical band gap of Y6-based films	12
Fig. S6. Cyclic voltammetry curves of PM6 and Y6-based films	12
Fig. S7. GIWAXS result of Y6-based films	13
Fig. S8. Orientation analysis of Y6-based films	13
Fig. S9. AFM images of 0.5%PM6:Y6 and 1.0%PM6:Y6	14
Fig. S10. PL spectra of Y6-based films	15
Fig. S12. Absorption features of Y6-based films	15
Fig. S12. Frequency-capacitance curves of 0.5%PM6:Y6	16
Fig. S13. IQE and EQE (CuSCN) curves of Y6-based devices	16
Fig. S14. SCLC measurements in PCE10:Y6-based devices	17
Fig. S15. EQE curves of Y6-based bilayer devices with different thicknesses	17
Fig. S16. PL spectra of N4-based films	18
Fig. S17. Optical band gap and Cyclic voltammetry curves of N4-based films	19
Fig. S18. SCLC and J_{SC} dependence of light intensity measurements in N4-based devices ...	20
Fig. S19. J_{ph}-V_{eff} curves of Y6 and N4 NHJ devices	20
Table S1. Photovoltaic performances of PM6:Y6 devices with different weight ratios	21
Table S2. Energy level of HOMO, LUMO and optical band gap of Y6-based films	21
Table S3. The fitted parameters from GIWAXS patterns for Y6-based films	21
Table S4. Summary of PL quenching efficiency of Y6-based films	22
Table S5. Mobility and trap state density of PM6:Y6-based devices	22
Table S6. Mobility and trap state density of PCE10:Y6-based devices	22
Table S7. Length of space-charge limited region of Y6-based devices	22
Table S8. Summarized delocalization-related parameters by DFT calculation	23
Table S9. Summary of PL quenching efficiency of N4-based films	23
Table S10. Photovoltaic performances of N4-based NHJ OSCs	23
Table S11. Energy level of HOMO, LUMO and optical band gap of N4-based NHJ OSCs ..	23
Table S12. Mobility of N4-based NHJ OSCs	24
Table S13. Summary of mobility ratio and Langevin pre-factor of N4-based NHJ OSCs	24

Experimental Section

Materials

Y6 was purchased from Solarmer Materials Inc. N4 was purchased from Nanjing Zhiyan Technology Co., Ltd. PM6 was purchased from Dongguan Volt-Amp Optoelectronics Tech. Co., Ltd. 3,3'-(1,3,8,10-Tetraoxoanthra[2,1,9-def:6,5,10-d'e'f] diisoquinoline-2,9(1H,3H,8H,10H)-diyl) bis (N,N-dimethylpropan-1-amine oxide) (PDINO) was purchased from Vizuchem. Chloroform (CF), methanol, and CuSCN were purchased from Sigma-Aldrich. Diethyl sulfide (DES) was purchased from Meryer. Phen-NaDPO was purchased from Zhengzhou Alfachem Inc. All chemicals were used as received without further purification.

Instrument

The current-voltage (J - V) curves were performed in the nitrogen-filled glove box under the illumination of AM 1.5G irradiation (100 mA/cm^2) with AAA solar simulator (SS-F5-3A, Enli Technology Co., Ltd.). Light intensity was calibrated with a standard photovoltaic cell with KG5 filter. The quantum efficiency was measured by Solar Cell Spectral Response Measurement System QE-R3018 (Enli Technology Co., Ltd.) with calibrated light intensity by a standard silicon cell. Photoluminescence (PL) spectra were recorded by FLS980 spectrometer (Edinburgh Instruments, EI). Absorption spectra were obtained on a Shimadzu UV-3600 Plus Spectrophotometer. The grazing-incidence wide-angle X-ray Scattering (GIWAXS) was performed at beamline 7.3.3 at the Advanced Light Source.¹ Films were spin-coated on silicon substrates with the same condition as device fabrication. The 10 keV X-ray beam was incident at a grazing angle of 0.12° and 0.14° . The scattered X-ray was detected using a Dectris Pilatus 2M photon counting detector. Atomic force microscope (AFM) images were obtained by Bruker INNOVA. Cyclic voltammetry and impedance spectrum tests were measured by PGSTAT 302N (Metrohm Autolab, Inc.). Illumination under different wavelengths was provided by an LED system (Thorlabs. Inc.).

Device fabrication

For the fabrication of NHJ and PM6:Y6 BHJ devices with a traditional device structure of ITO/PEDOT:PSS (Heraeus Clevios PVP Al 4083)/active layer/PDINO/Al, the patterned ITO substrates were cleaned by deionized water, acetone, and isopropanol sequentially. Then the pre-cleaned ITO was treated in an ultraviolet ozone generator for 15 min, followed by spin-coating PEDOT:PSS solution on substrates at 5500 rpm for 30 s. After thermal annealing at 150°C for 30 min, the substrates were transferred into a glove box. The Y6 (15 mg/mL), N4

(15 mg/mL) and PM6 (1 mg/mL) were dissolved in chloroform (CF) solvent and stirred on the hot plate at 50 °C for more than an hour. Different volume of PM6 was added to acceptor solutions later. After that, the solutions were spin-coated on PEDOT:PSS to obtain a similar thickness of 90 nm \pm 5 nm. The PM6:Y6 (16 mg/mL, D:A=1:1.2) were dissolved in CF solvent and stirred on the hot plate at 50 °C for more than an hour, followed by spin-coating on PEDOT:PSS at 3000 rpm to get films at thickness about 100 nm. Then a PDINO layer (2 mg/mL in methanol, 3300 rpm for 30 s) was spin-coated on the active layer. Finally, 100 nm Al was deposited by thermal evaporation as the electrode at a vacuum level under 5×10^{-4} Pa.

For the fabrication of devices with inverted structure of ITO/ZnO/active layer/MoO₃/Al, the ZnO precursor solution was first spin-coated on the substrate at 4500 rpm for 30 s, followed by thermal annealing at 200 °C for 30 min. After spin-coating the active layer in the glove box as mentioned above, a thin layer of 10 nm MoO₃ and 100 nm Al was deposited by thermal evaporation at a vacuum level under 5×10^{-4} Pa as the hole transporting layer and the electrode, respectively.

For the fabrication of bilayer devices to calculate the L_{EX+CS} , the patterned ITO substrates were first cleaned the same as above. CuSCN (25 mg/ml) was dissolved in DES at 60 °C for 1 h and filtered. Then the CuSCN solution was spin-coated on ITO substrates at 2000 rpm for 30 s, followed by annealing at 105 °C for 10 min to obtain thin films with thickness ca. 50 nm. Y6 and 1.0%PM6:Y6 solutions were prepared as mentioned above with different concentrations (3-20 mg/ml) and were spin-coated on the CuSCN layer for 30 s to obtain film thicknesses ranging from 8 nm to 150 nm. Next, a layer of ca. 5 nm of Phen-NaDPO as an electron-transport layer (ETL) and exciton blocking layer (EBL) was spin-coated from methanol solution (0.5 mg/ml) on top of the active layer. Finally, 100 nm Al was deposited by thermal evaporation as the anode at a vacuum level under 5×10^{-4} Pa.

Calculation of J_{max} ²⁻⁴

The simulated exciton generation profiles and the theoretical limit of photo-current density were obtained by the transfer-matrix modeling. The model divided the device structure into multiple thin sub-layers, and the extinction coefficient k of each sub-layer can be calculated from the absorption spectra according to the Kramers-Kronig relationship. The refractive index n is set to 2 for organic semiconductors since their values pose little impact on the simulated result. Then electric field $E(x)$ at an arbitrary position x in the direction of charge transport can be calculated according to previous reports, and the exciton generation profiles $G(x)$ can be obtained by:

$$G(x) = \int_{\lambda_1}^{\lambda_2} \text{IQE} \cdot \frac{2\pi\epsilon_0 kn}{\hbar} |E(x)|^2 d\lambda \quad (\text{S1})$$

where, IQE is the internal quantum efficiency and set to unity, \hbar is the Planck constant, ϵ_0 is the vacuum permittivity, λ_1 and λ_2 are the upper and lower limits of the integrated wavelength range. They are set to 400 nm and 1000 nm when calculating the theoretical maximum current density (J_{max}). These two parameters are set to 400 nm and 600 nm when calculating the theoretical limit when considering the contribution of spontaneous photo-charge generation only ($J_{\text{max,sp}}$). Finally, integrating $G(x)$ through the active layer gives the corresponding photo-current value.

Cyclic voltammetry measurements

The positions of the HOMO and LUMO were determined by cyclic voltammetry measurements. The specific values can be calculated from the following equations:

$$E_{\text{HOMO}} = -e(E_{\text{ox}} - E_{\text{Fe}} + 4.8) \quad (\text{S2})$$

$$E_{\text{LUMO}} = -e(E_{\text{red}} - E_{\text{Fe}} + 4.8) \quad (\text{S3})$$

where, E_{ox} is the initial oxidation potential, E_{red} is the initial reduction potential, and E_{Fe} is the average value between oxidation potential and reduction potential of Ferrocene.

Impedance measurements^{5,6}

The structure of devices is ITO/PEDOT:PSS/active layer/PDINO/Al diode. Capacitance-frequency spectrum was performed at zero bias and a frequency range of 100 Hz to 1 MHz with illumination provided by an LED at about 50 mW/cm². Capacitance can be calculated through the complex impedance with the equation of

$$C_p = -\frac{1}{\omega} \left[\frac{Z'' - \omega L}{(Z' - R_s)^2 + (Z'' - \omega L)^2} \right] \quad (\text{S4})$$

where, Z' and Z'' represent the real and imaginary part of the complex impedance, ω is the angular frequency ($\omega = 2\pi f$), f is the AC signal frequency, L is the inductance of wires (6×10^{-6} H), and R_s is the AC series resistance extracted from the real impedance saturated in the high frequency.

Geometric capacitance (C_g) of the active layer is frequency-independent and can be obtained from the C_p value at 10⁵ Hz; and C_{in} at 100 Hz can be calculated by subtracting C_g (10⁵ Hz) from C_p (100 Hz, Equation (S5)). Then the corresponding photo-charge density (n) at short-circuit condition can be calculated by Equation (S6):

$$C_{\text{in}} = C_p - C_g \quad (\text{S5})$$

$$n = \frac{1}{qAd} C_{sat} (V_0 - V_{sat}) + \frac{1}{qAd} \int_{V_{sat}}^0 C_{in} dV \quad (S6)$$

where, A and d are the area and thickness of the active layer. V_{sat} is the voltage when the photo-current reaches its saturation at reverse bias. C_{sat} is the capacitance of the active layer at V_{sat} . V_0 is the forward bias at which the photocurrent is equal to zero.

To obtain the photo-charge density ratio between Y6- and N4-only NHJ OSC, two methods are applied in this work for simplified calculation. First, V_{sat} is assumed to be the same because it is difficult for NFA-only devices to reach the saturation of photo-current and a large reverse bias larger than 5 V is needed. As a result, the variation of V_0 compared to twofold V_{sat} is negligible (Fig. S19). Second, C_{in} under reverse bias is assumed to be the same as the value at short-circuit condition since C_{in} under reverse bias is usually more stable than under forward bias as reported. Now Equation (S6) can be written as follows, and n is linearly dependent on C_{in} .

$$n = \frac{1}{qAd} C_{in} (V_0 - 2V_{sat}) \propto C_{in} \quad (S7)$$

Mott-Schottky relation was used to obtain the built-in voltage (V_{bi}) of the devices (Equation (S8)), and the length of the space-charge region (L_S) can be calculated according to Equation (S9).

$$\frac{1}{C^2} = \frac{2}{q\epsilon_0\epsilon_r N_t} (V_{bi} - V) \quad (S8)$$

$$L_S = \frac{\epsilon_0\epsilon_r}{C} = \sqrt{\frac{2\epsilon_0\epsilon_r}{qN_t} (V_{bi} - V)} \quad (S9)$$

where, ϵ_0 is the vacuum permittivity, ϵ_r is the relative dielectric constant of the active layer and assumed to be 3 for all the conditions.

Space charge limited current (SCLC) characteristics^{7, 8}

Hole-only devices were fabricated with ITO/PEDOT:PSS/active layer/MoO₃/Al structures, electron-only devices were fabricated with ITO/ZnO/active/PDINO/Al structures and double-carrier devices were fabricated with ITO/PEDOT:PSS/active layer/PDINO/Al structures. The values of SCLC mobility are obtained by fitting the J - V curves according to:

$$J = \frac{9}{8} \epsilon_0 \epsilon_r \mu \frac{V^2}{d^3} \quad (S10)$$

where ϵ_0 is the vacuum permittivity, ϵ_r is the relative permittivity of the active layer and it is assumed to be 3 here, d is the thickness of the active layer.

The trap state density (n_t) can be calculated by the formulation of: $V_{TFL} = (en_t d^2)/(2\varepsilon_r \varepsilon_0)$. The V_{TFL} is the trap-filled limit voltage and can be obtained at the transition from the ohmic region into the trap-filled limit region, d is the thickness of the active layer, ε_0 is the vacuum permittivity, ε_r is the relative dielectric constant and e is the elementary charge.

The Langevin pre-factor (γ_{pre}) can be calculated through the hole mobility (μ_h), electron mobility (μ_e) and double-carrier mobility (μ_{eff}) with the following equation:

$$\gamma_{pre} = \frac{16\pi}{9} \frac{\mu_p \mu_n}{\mu_{eff}^2 - (\mu_p + \mu_n)^2} \quad (S11)$$

Calculation of L_{EX+CS} ⁹⁻¹¹

According to the reports, CuSCN provides a bilayer interface with the active layer that boosts effective exciton quenching and collection of spontaneously formed photo-charges, while the Phen-DPO extracts electrons and reflects all the excitons at the same time. As a result, overall EQE response mostly comes from the excitons and holes reaching the CuSCN/active layer interface. Adjusting the thickness of the active layer and measuring the EQE allow the study of exciton/carrier hybrid diffusion length (L_{EX+CS}).

The EQE spectra of bilayer devices with a series film thickness can be modeled by a one-dimension exciton diffusion equation:

$$\frac{\partial n(x,t)}{\partial t} = D \frac{\partial^2 n(x,t)}{\partial x^2} + G(x,t) - k_r n(x,t) - k_{FRET} n(x,t) - \gamma n(x,t)^2 \quad (S12)$$

where, $G(x, t)$ is the time-dependent exciton generation profile at position x given by transfer matrix modeling, k_r is the radiative decay rate without quencher sites, γ is an exciton-exciton annihilation rate constant, and k_{FRET} denotes the rate of Forster energy transfer (FRET) in the presence of a neighboring material. As FRET between CuSCN and the active layer is negligible owing to the small overlap between the absorption spectra of CuSCN and the emission spectra of the active layer, k_{FRET} is zero. Due to the small light intensity during EQE measurements, γ is also regarded as zero. Hence, Equation S(12) can be simplified under steady-state conditions

$k_r = D / L_{EX+CS}^2$ as

$$\left(\frac{\partial^2}{\partial x^2} - \frac{1}{L_{EX+CS}^2} \right) n(x) = -\frac{G(x)}{D} \quad (S13)$$

The general solution of Equation (S13) can be written as:

$$Dn(x) = \left[k_1 - \frac{L_{EX+CS}}{2} \int_d^x e^{-x'/L_{EX+SP}} G(x') dx' \right] e^{x/L_{EX+CS}} + \left[k_2 + \frac{L_{EX+CS}}{2} \int_d^x e^{x'/L_{EX+SP}} G(x') dx' \right] e^{-x/L_{EX+CS}} \quad (S14)$$

k_1 and k_2 are constants and can be solved with boundary conditions of complete exciton quenching at the active layer/CuSCN interface ($n=0$) and complete exciton reflection at the active layer/Phen-DPO interface ($\partial n/\partial x=0$). So, they are given as:

$$k_1 = -k_2 e^{-2d/L_{EX+CS}} \quad (S15)$$

$$k_2 = \frac{-\frac{L_{EX+CS}}{2} \int_d^0 e^{-x'/L_{EX+CS}} G(x') dx' - \frac{L_{EX+CS}}{2} \int_d^0 e^{x'/L_{EX+CS}} G(x') dx'}{e^{-2d/L_{EX+CS}} + 1} \quad (S16)$$

The EQE can then be obtained considering that the photocurrent comes from the hole extraction and the exciton dissociation at the active layer/CuSCN interface:

$$EQE = \frac{J_{photo}}{J_{inc}} = \frac{q\eta}{J_{inc}} \frac{D\partial n(x)}{\partial x} \Big|_{interface} \quad (S17)$$

where, J_{photo} and J_{inc} are the generated photocurrent density and the incident light current density, η is the total efficiency of exciton dissociation and charge collection. The shape of the normalized EQE vs. thickness curve is determined by $D\partial n(x)/\partial x$, which is given by

$$\frac{D\partial n(x)}{\partial x} (x=d) = \frac{1}{L_{EX+CS}} e^{\frac{x}{L_{EX+CS}}} k_1 - \frac{1}{L_{EX+CS}} e^{\frac{-x}{L_{EX+CS}}} k_2 \quad (S18)$$

The calculation is written in MATLAB language.

DFT calculation¹²⁻¹⁴

All DFT calculation was carried out using the ORCA 5.0.0. software package. The gas-phase ground-state geometry optimizations were performed at RI-B3LYP-D3(BJ)/def2-TZVP level. The density functional dispersion correction was conducted by Grimme's D3 version with Becke–Johnson damping function. The TD-DFT calculation was adopted using the PBE0 functional, along with the orbital expansion basis set def2-TZVP to optimize geometries of excited states. Based on the results of TD-DFT calculation, hole–electron analysis was performed and visualized using the Multiwfn 3.8 dev and VMD 1.9.3 software package.

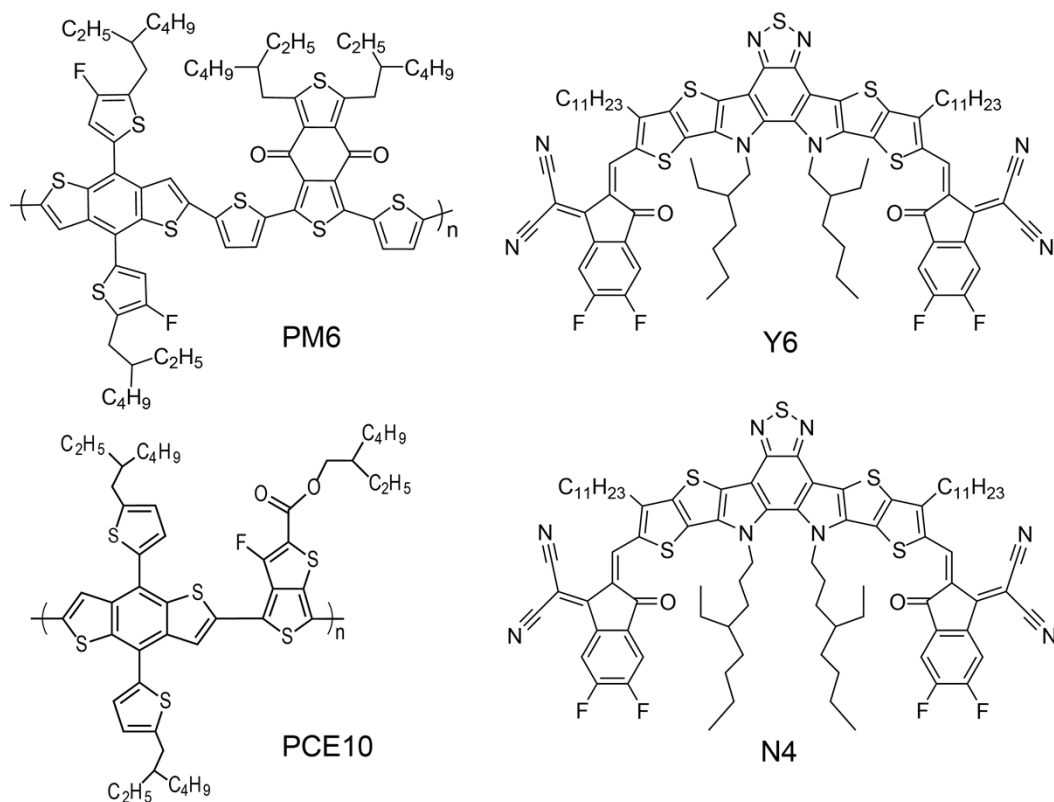


Fig. S1. Chemical structure of Poly[(2,6-(4,8-bis(5-(2-ethylhexyl-3-fluoro)thiophen-2-yl)-benzo[1,2-b:4,5-b']dithiophene))-alt-(5,5-(1',3'-di-2-thienyl-5',7'-bis(2-ethylhexyl)benzo[1',2'-c:4',5'-c']dithiophene-4,8-dione)] (PM6), Poly[4,8-bis(5-(2-ethylhexyl)thiophen-2-yl)benzo[1,2-b;4,5-b']dithiophene-2,6-diyl-alt-(4-(2-ethylhexyl)-3-fluorothieno[3,4-b]thiophene-)-2-carboxylate-2,6-diyl] (PCE10), 2,2'-((2Z,2'Z)-((12,13-bis(2-ethylhexyl)-3,9-diundecyl-12,13-dihydro-[1,2,5]thiadiazolo[3,4-e]thieno[2'',3''':4',5']thieno[2',3':4,5]pyrrolo[3,2-g]thieno[2',3':4,5]thieno[3,2-b]indole-2,10-diyl)bis(methanylylidene))bis(5,6-difluoro-3-oxo-2,3-dihydro-1H-indene-2,1-diylidene))dimalononitrile (Y6), 2,2'-((2Z,2'Z-(12,13-bis(4-ethyloctyl)-3,9-diundecyl-12,13-dihydro-[1,2,5]thiadiazolo[3,4-e]thieno[2'',3''':4',5']thieno-[2',3':4,5]pyrrolo[3,2-]thieno[2',3':4,5]thieno[3,2-b]indole-2,10-diyl) bis(methanylylidene))bis(5,6-difluoro-3-oxo-2,3-dihydro-1H-indene-2,1-diylidene))dimalononitrile (N4).

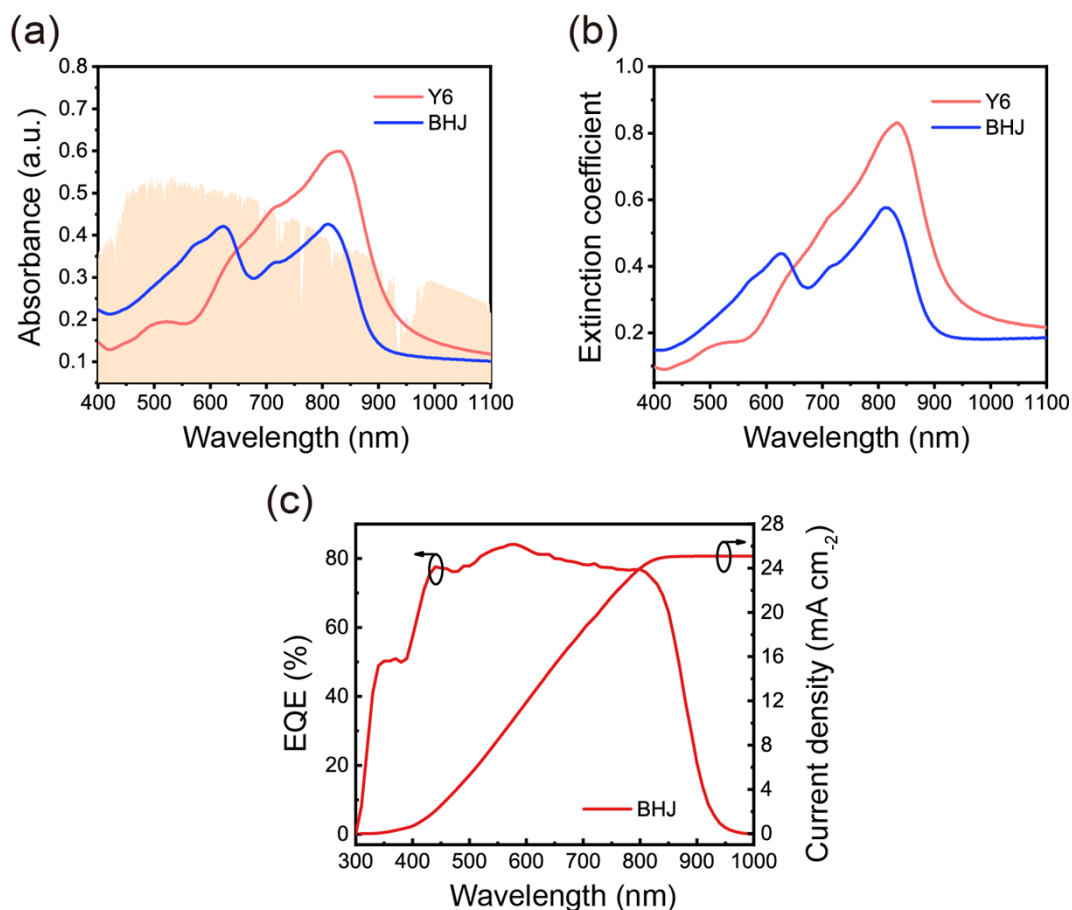


Fig. S2 (a) Absorbance of Y6 and PM6:Y6 BHJ film. The shadow area marks the AM 1.5G solar spectrum. (b) Extinction coefficient of Y6 and PM6:Y6 BHJ film. (c) EQE and corresponding integrated current density curves of PM6:Y6 BHJ device.

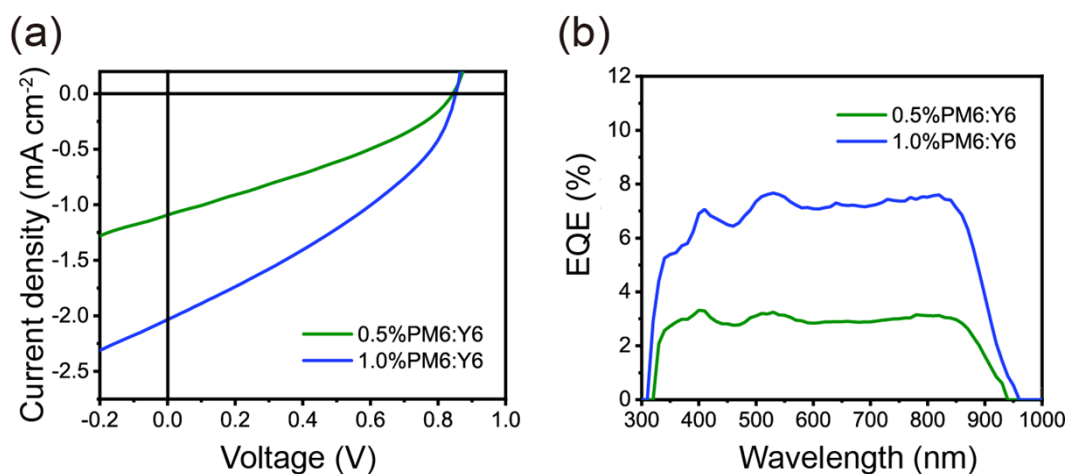


Fig. S3. (a-b) J - V and EQE curves of 0.5%PM6:Y6 and 1.0%PM6:Y6 with traditional device structure when PEDOT:PSS acts as hole-transporting layer.

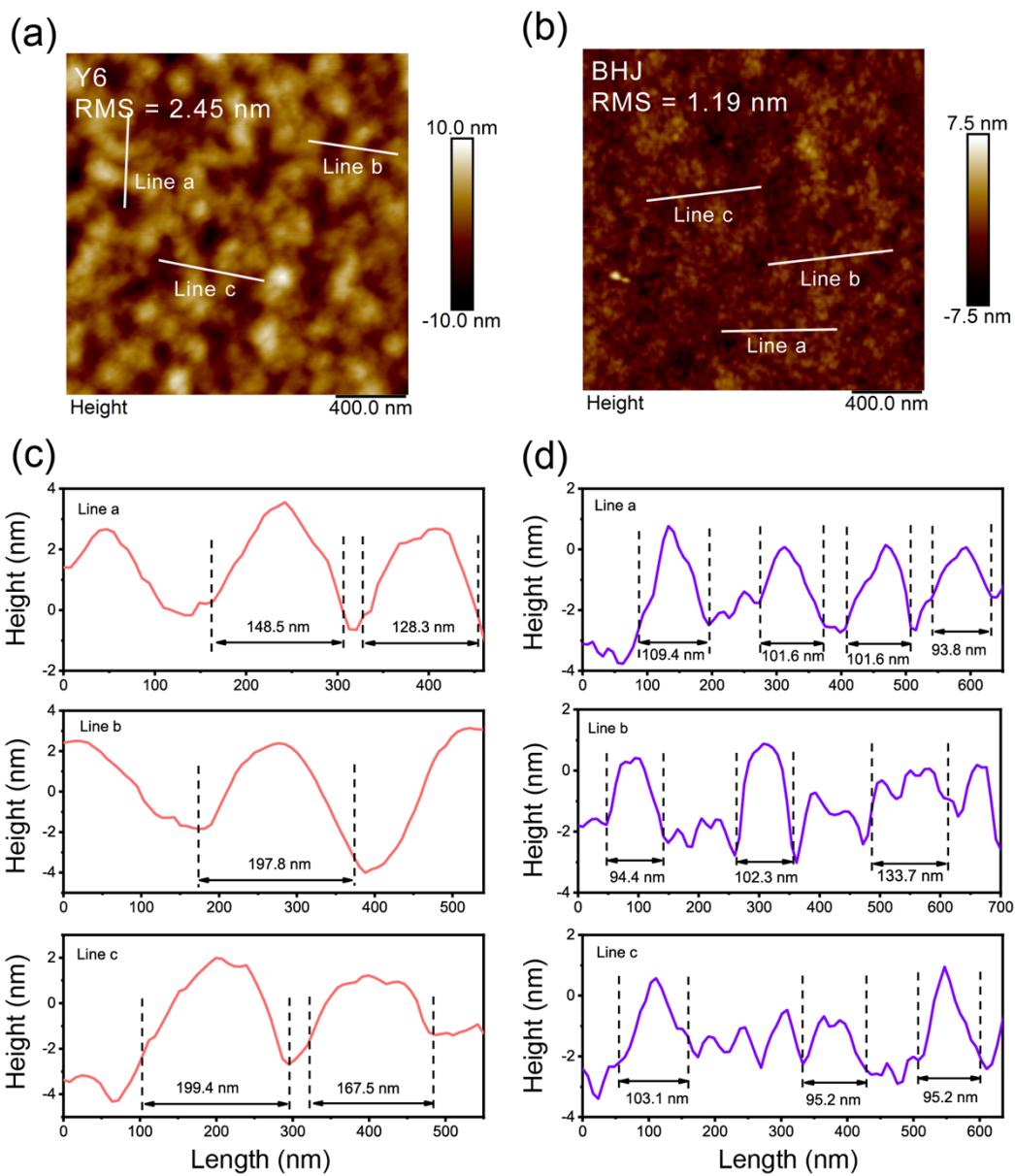


Fig. S4. (a-b) AFM image of Y6 and PM6:Y6 BHJ film. (c-d) Line profiles to obtain the fiber width of Y6 and PM6:Y6 BHJ film.

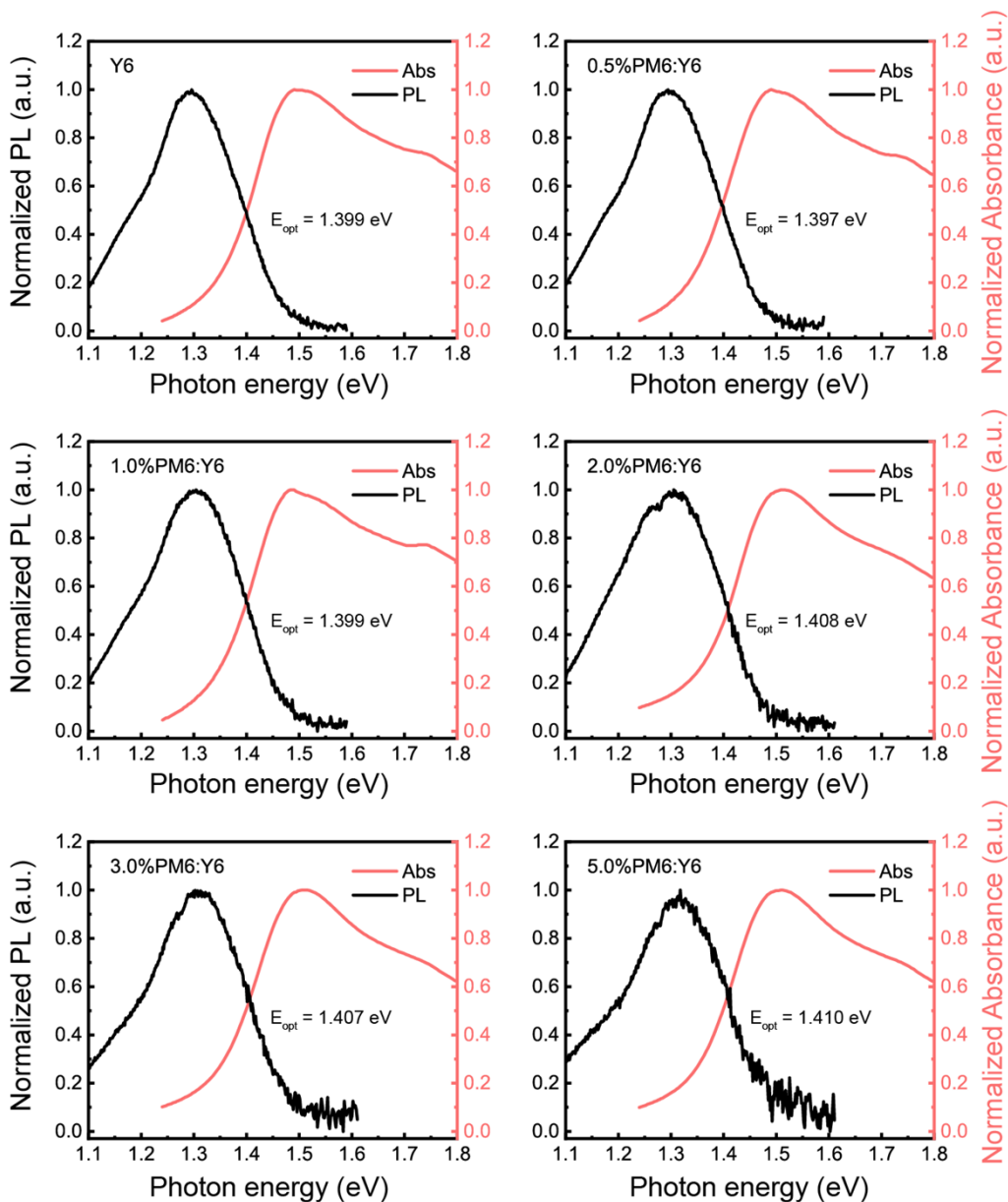


Fig. S5. Optical band gap obtained from the intersection point of normalized absorption and photoluminescence spectra of Y6 blended with various amounts of PM6.

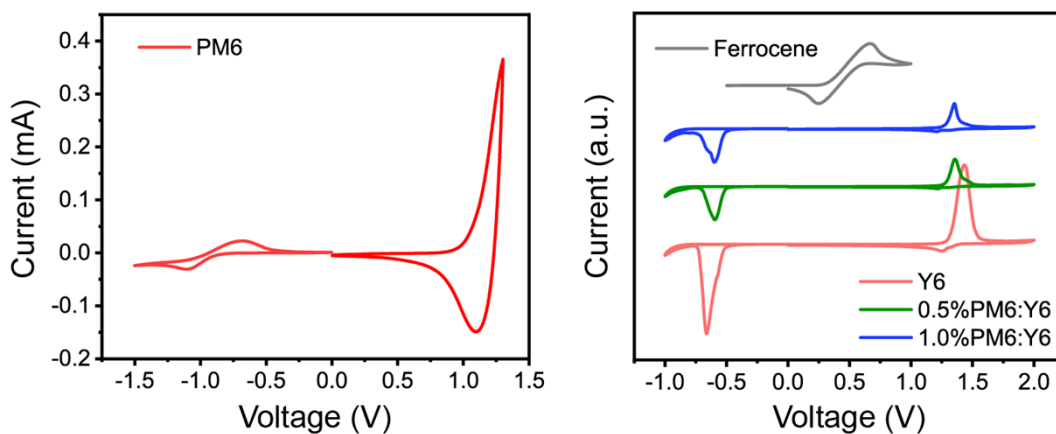


Fig. S6. Cyclic voltammety curves of PM6, Y6 and its blend with various amounts of PM6.

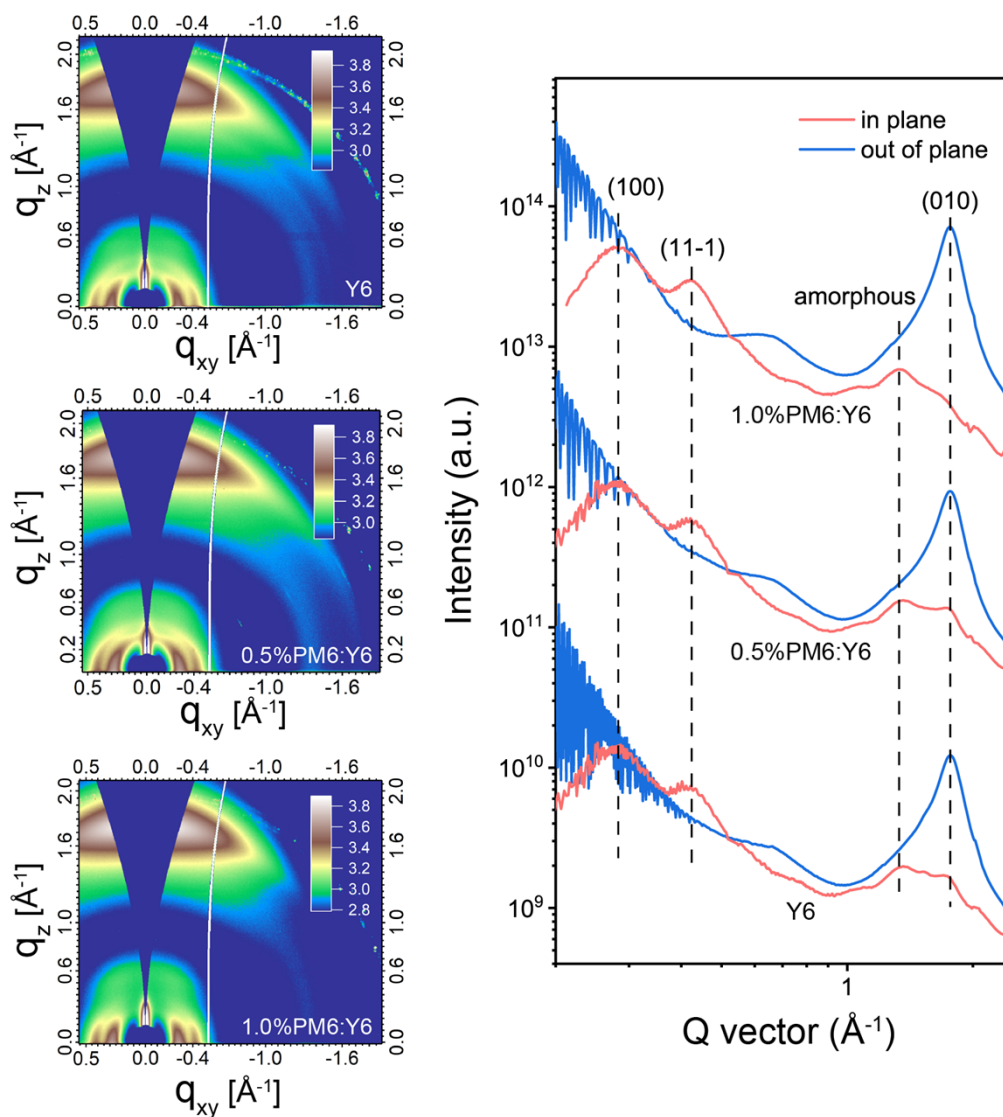


Fig. S7. 2D GIWAXS scattering patterns and 1D line-cuts of Y6 pure film and its blend with various amounts of PM6.

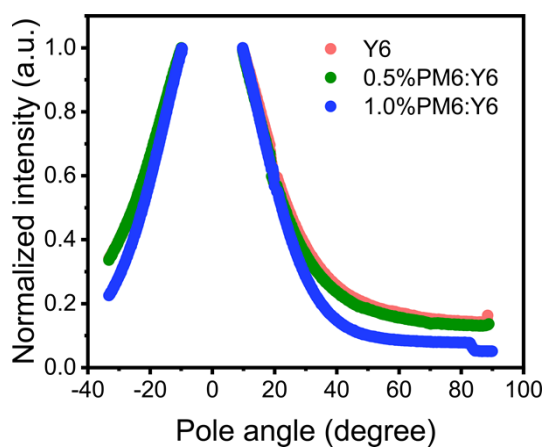


Fig. S8. Pole figures of (010) diffraction peaks for Y6 pure film and its blend with various amounts of PM6

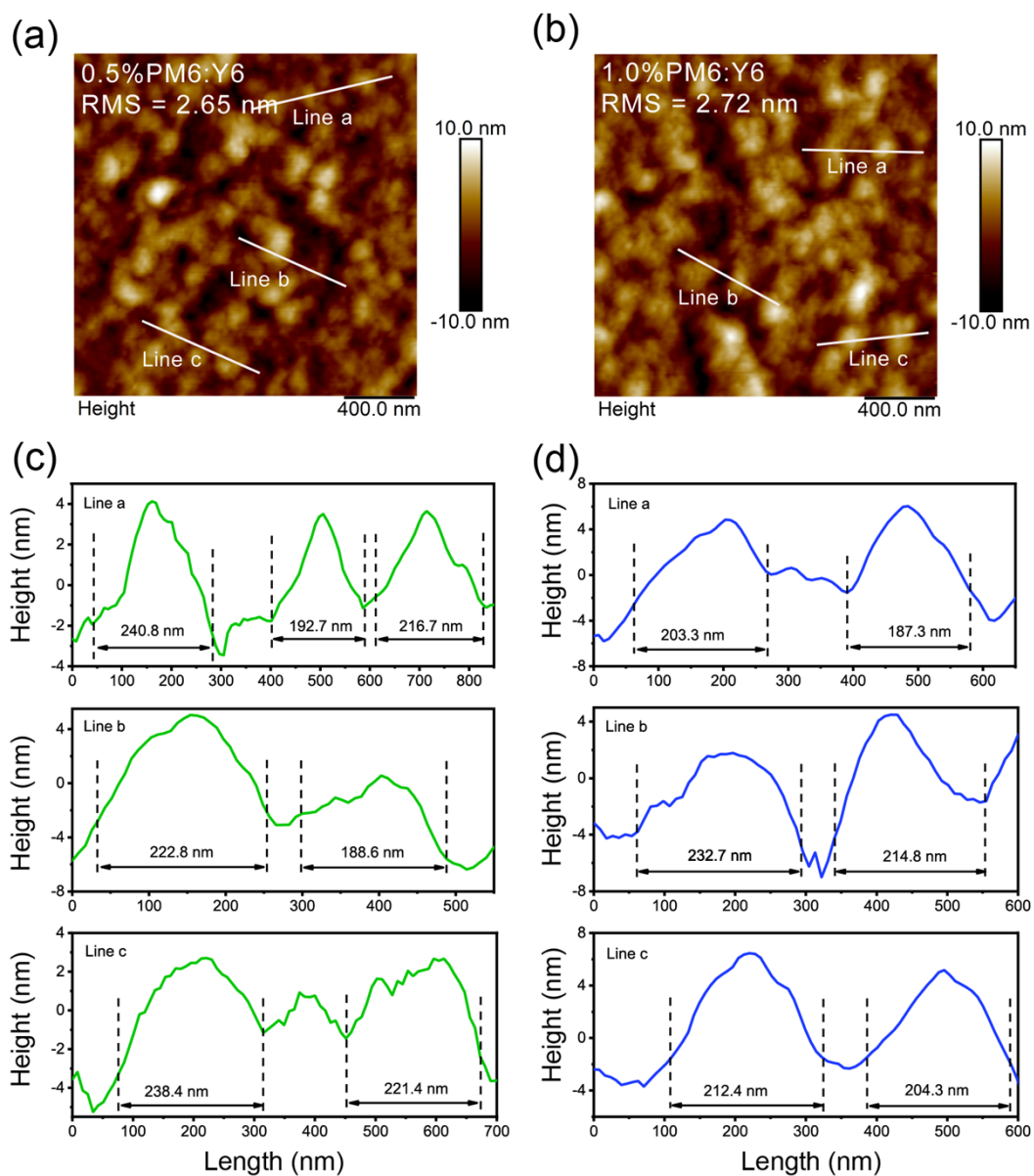


Fig. S9. (a-b) AFM image of 0.5%PM6:Y6 and 1.0%PM6:Y6 film. (c-d) Line profiles to obtain the fiber width of 0.5%PM6:Y6 and 1.0%PM6:Y6 BHJ film.

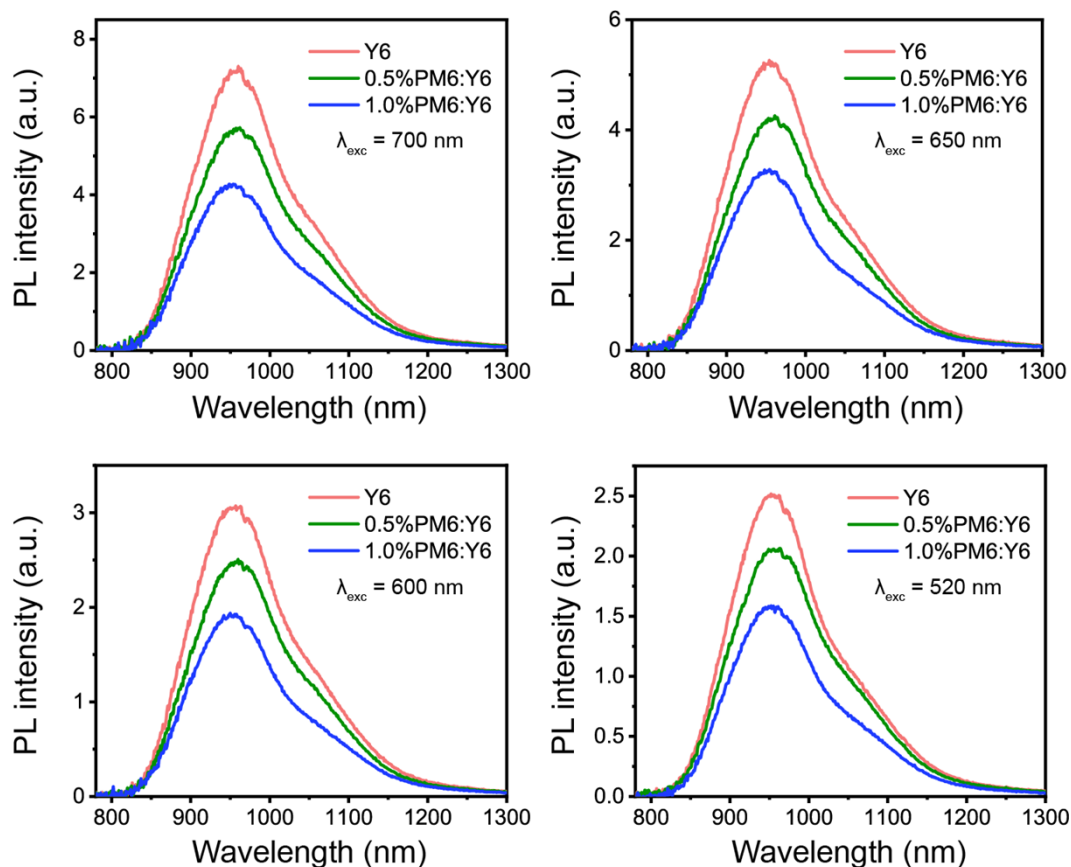


Fig. S10. PL spectra of Y6 pure film and its blend with various amounts of PM6 under different exciting wavelengths (700 nm, 650 nm, 600 nm and 520 nm).

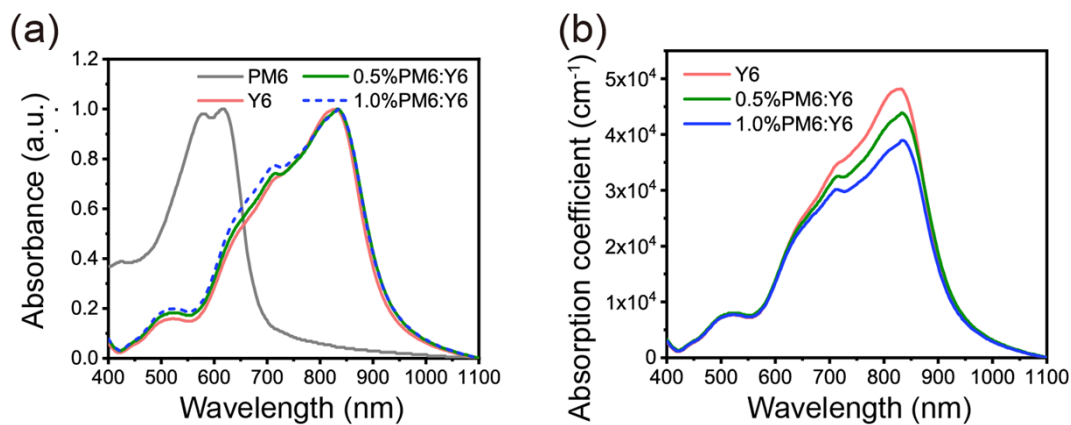


Fig. S11. (a) Normalized absorption spectra of PM6, Y6 pure films and Y6 blended with various amounts of PM6. (b) Absorption coefficients of Y6 pure films and its blend with various amounts of PM6.

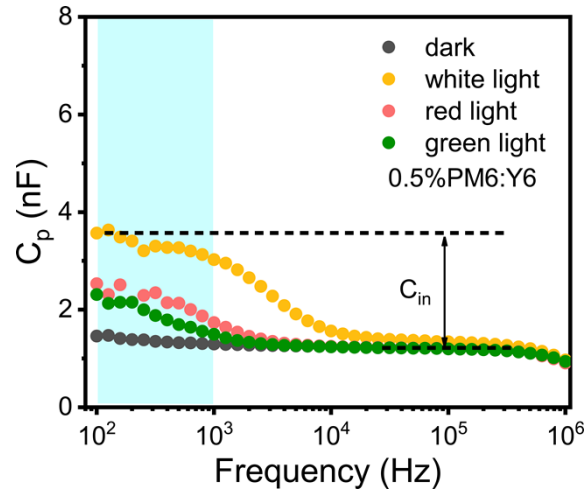


Fig. S12. Frequency-dependent capacitance spectra of 0.5%PM6:Y6 under dark conditions, 50 mA/cm² white (300~700 nm), red (660 nm) and green (565 nm) light LED illumination. Blue shadow marks the frequency range where chemical capacitance (C_{in}) dominates and the C_{in} under white light illumination is marked.

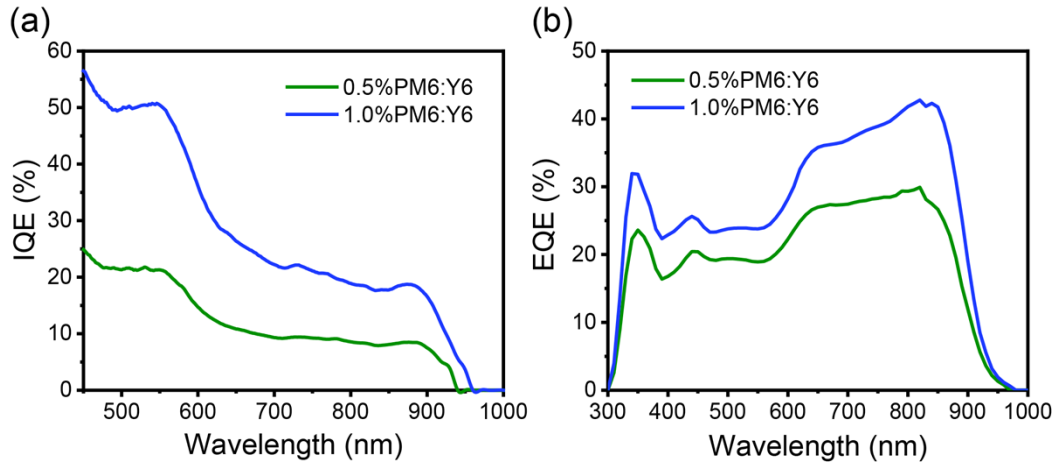


Fig. S13. (a) IQE curves of 0.5%PM6:Y6 and 1.0%PM6:Y6 when PEDOT:PSS acts as the hole-transporting layer. (b) EQE curves of 0.5%PM6:Y6 and 1.0%PM6:Y6 when CuSCN acts as the hole-transporting layer.

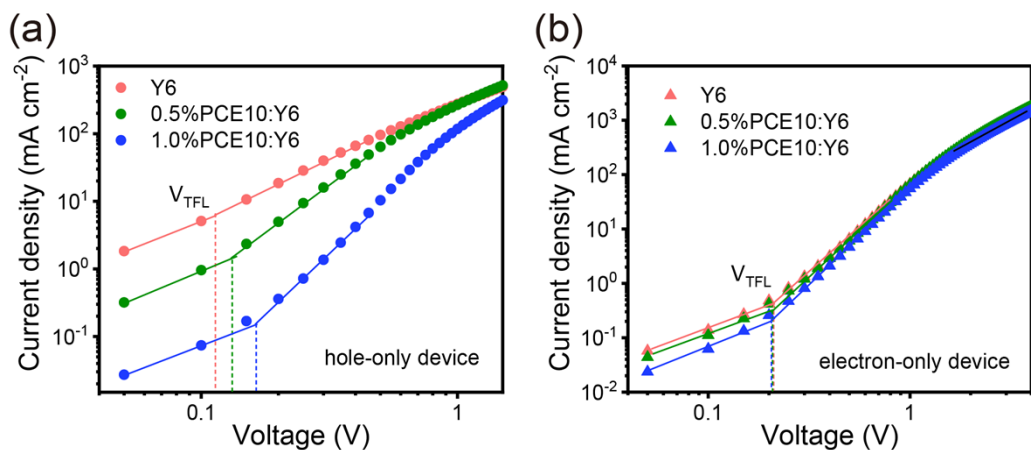


Fig. S14. (a-b) Hole-only and electron-only current density versus voltage curves of Y6, 0.5%PCE10:Y6 and 1.0%PCE10:Y6. Dashed lines mark the position of trap-filled limit voltage (V_{TFL}) on the voltage axis

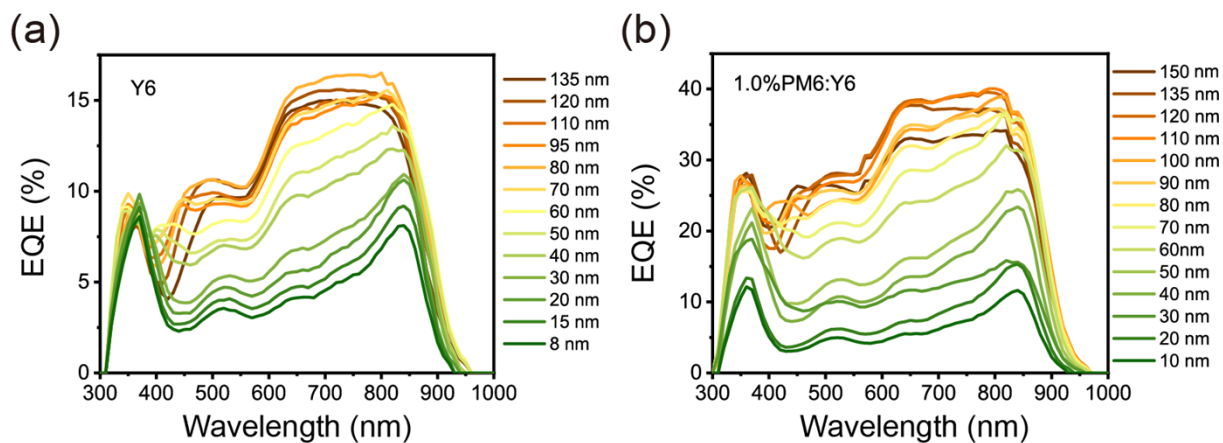


Fig. S15. (a-b) EQE curves of Y6/CuSCN and 1.0%PM6:Y6/CuSCN devices with different active layer thicknesses.

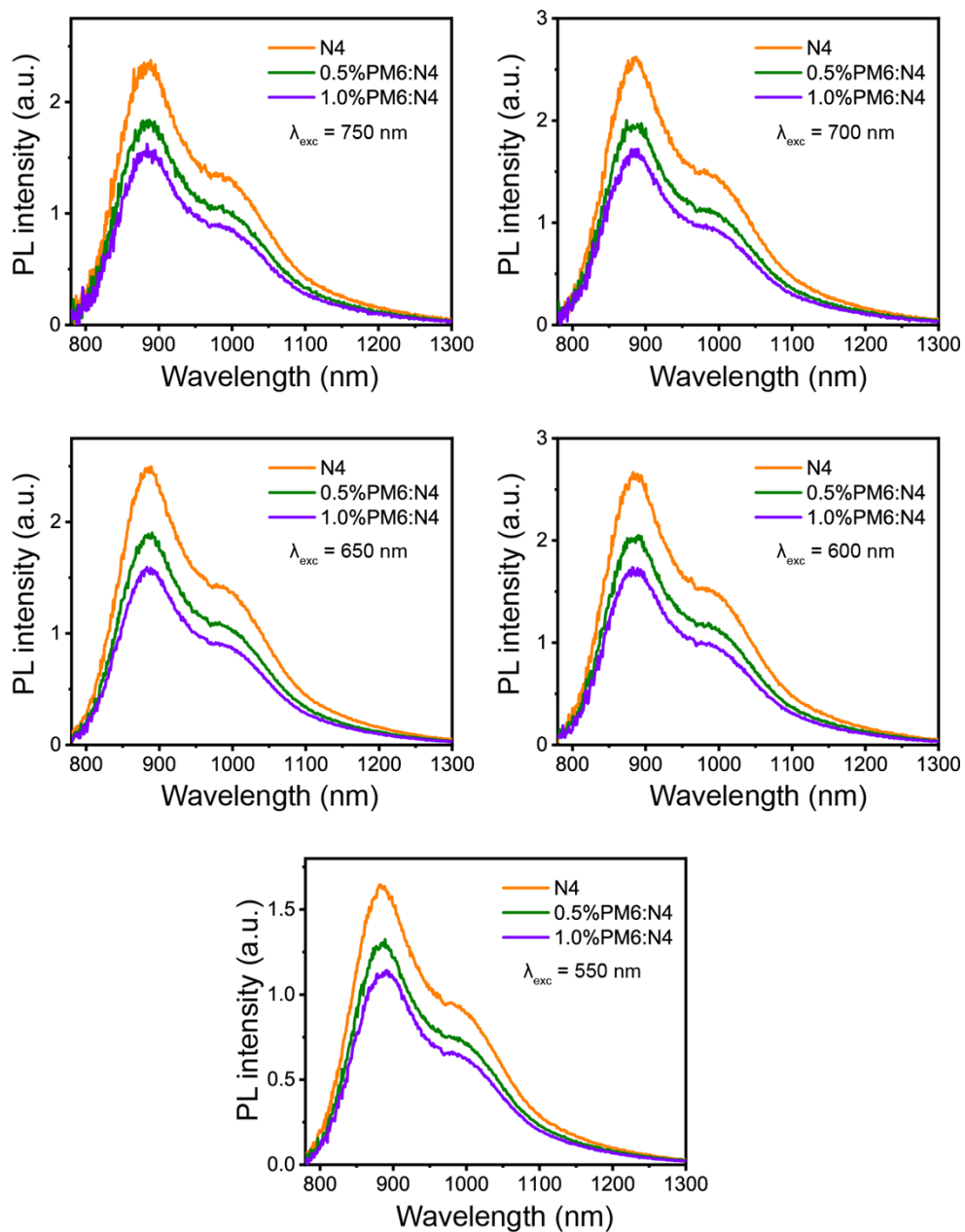


Fig. S16. PL spectra of N4 pure film and its blend with various amounts of PM6 under different exciting wavelengths (750 nm, 700 nm, 650 nm, 600 nm and 550 nm).

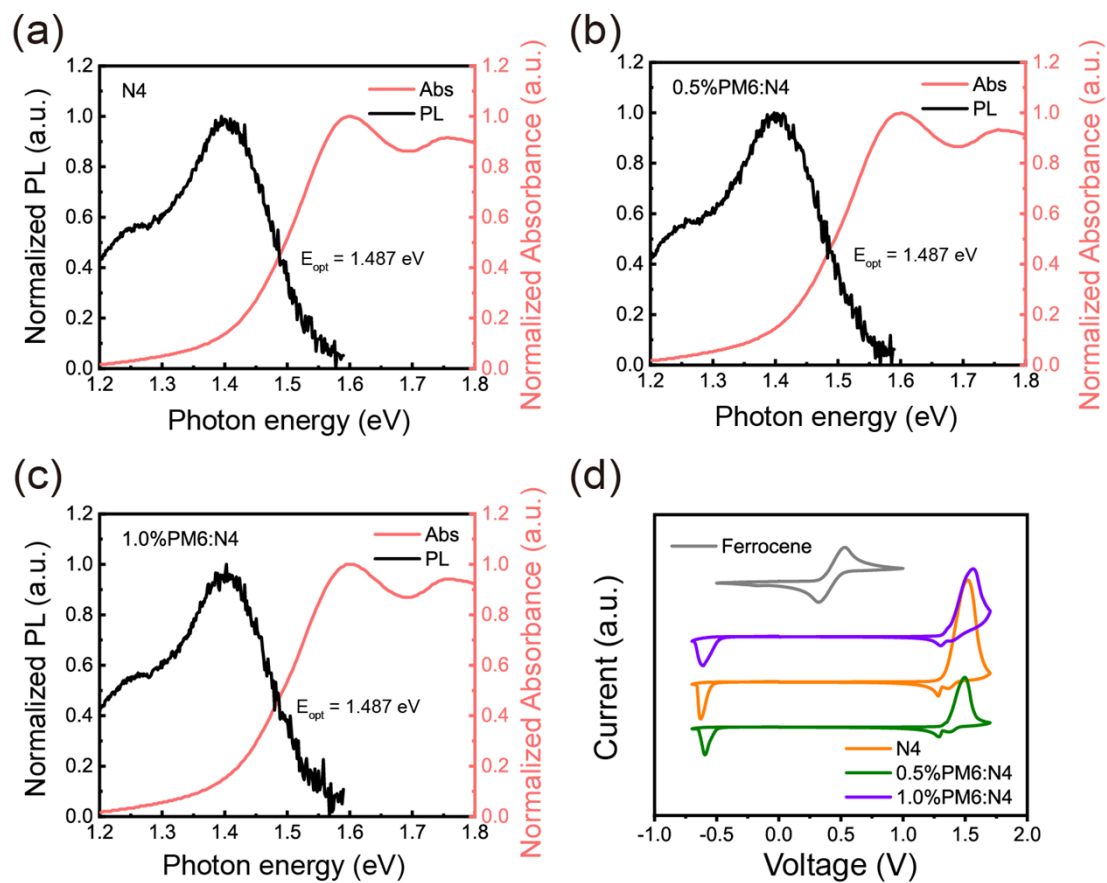


Fig. S17. (a-c) Optical band gap obtained from the intersection point of normalized absorption and PL spectra of N4 blended with various amounts of PM6. (d) Cyclic voltammetry curves of N4 and its blend with various amounts of PM6.

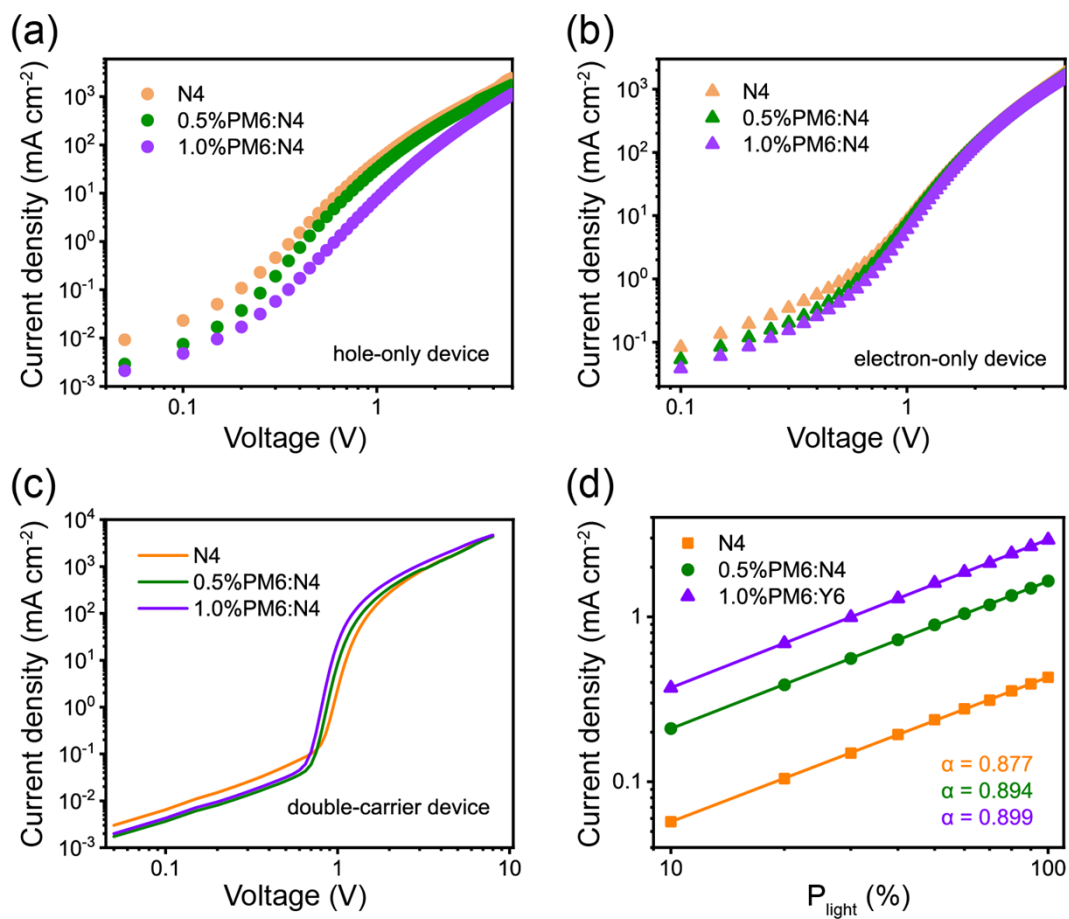


Fig. S18. (a-c) Hole-only, electron-only, and double-carrier current density versus voltage curves of N4-based devices. (d) Curves of J_{SC} dependence on light intensity in N4-based devices.

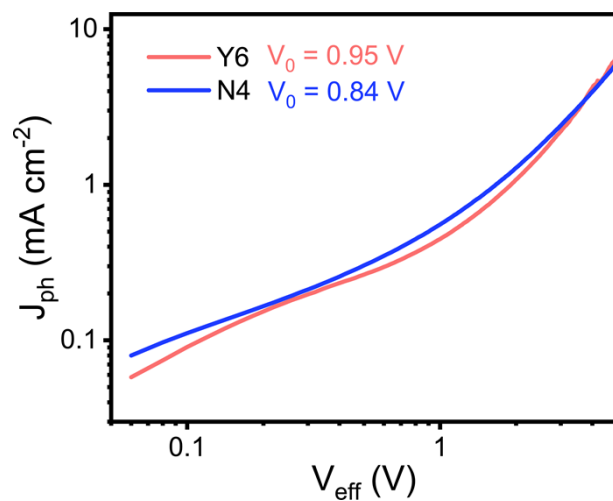


Fig. S19. J_{ph} - V_{eff} curves of Y6 and N4 NHJ devices.

Table S1. Photovoltaic performance of PM6:Y6 OSCs with various weight ratios. ^a

Ratio	V_{OC} (V)	FF (%)	J_{SC} (mA cm ⁻²)	PCE (%)	J_{SC} (EQE) (mA cm ⁻²)
0:1	0.833 (0.826±0.012)	28.57 (27.88±0.98)	0.28 (0.24±0.02)	0.07 (0.06±0.01)	/
0:1 (inverted)	0.420 (0.385±0.014)	40.59 (39.20±0.85)	0.23 (0.22±0.01)	0.04 (0.03±0.00)	/
0.005:1	0.844 (0.837±0.006)	33.46 (31.89±0.96)	1.09 (0.94±0.13)	0.31 (0.25±0.04)	1.003
0.01:1	0.848 (0.839±0.009)	36.45 (35.65±0.47)	2.45 (2.25±0.12)	0.76 (0.67±0.04)	2.421
1:1.2	0.868 (0.861±0.004)	72.32 (71.33±0.53)	26.40 (26.09±0.25)	16.31 (16.08±0.12)	25.09

^a The maximum and average values were obtained from more than 10 independent devices.

Table S2. Summary of HOMO, LUMO and optical band gap of PM6, Y6 pure films and blended with various amounts of PM6.

Materials	HOMO (eV)	LUMO (eV)	E_{opt} (eV)
PM6	-5.50	-3.43	/
Y6	-5.60	-3.80	1.399
0.5%PM6:Y6	-5.59	-3.82	1.397
1.0%PM6:Y6	-5.61	-3.82	1.399

Table S3. The fitted peak position, d-spacing, FWHM and coherence length (CL) from GIWAXS pattern for Y6 pure films and blended with various amounts of PM6.

Materials	Location (Å ⁻¹)	d-spacing (Å)	FWHM	CL (nm)	Location (Å ⁻¹)	d-spacing (Å)	FWHM	CL (nm)
Y6	0.279	22.499	0.101	5.590	1.762	3.566	0.208	2.723
	0.416	15.118	0.184	3.065	1.386	4.533	0.502	1.126
0.5%PM6:Y6	0.286	21.944	0.081	7.023	1.744	3.604	0.196	2.885
	0.415	15.123	0.136	4.161	1.367	4.597	0.294	1.925
1.0%PM6:Y6	0.284	22.160	0.077	7.327	1.725	3.642	0.184	3.071
	0.414	15.186	0.123	4.597	1.336	4.702	0.203	2.788

Table S4. PL quenching efficiency (PLQE) of 0.5%PM6:Y6 and 1.0%PM6:Y6 under different exciting wavelengths.

λ_{exc} (nm)	PLQE _{0.5%}	PLQE _{1.0%}	PLQE _{1.0%} / PLQE _{0.5%}
750	0.189	0.391	2.069
700	0.189	0.396	2.095
650	0.180	0.375	2.083
600	0.179	0.376	2.101
550	0.130	0.356	2.738
520	0.141	0.362	2.567

Table S5. Mobility, trap-filled limit voltage and trap state density of Y6 blended with various amounts of PM6. ^a

Materials	μ_{h} ($10^{-4}\text{cm}^2\text{V}^{-1}\text{s}^{-1}$)	μ_{e} ($10^{-4}\text{cm}^2\text{V}^{-1}\text{s}^{-1}$)	$V_{\text{TFL,h}}$ (V)	$n_{\text{t,h}}$ (10^{15}cm^{-3})	$V_{\text{TFL,e}}$ (V)	$n_{\text{t,e}}$ (10^{16}cm^{-3})
Y6	6.98±0.53	1.75±0.04	0.113	5.85	0.275	1.43
0.5%PM6:Y6	4.85±0.50	1.79±0.05	0.127	6.68	0.260	1.35
1.0%PM6:Y6	2.57±0.26	1.83±0.06	0.148	7.67	0.267	1.38

^a The average values were obtained from more than 5 independent devices.

Table S6. Mobility, trap-filled limit voltage and trap state density of Y6 blended with various amounts of PCE10. ^a

Materials	μ_{h} ($10^{-4}\text{cm}^2\text{V}^{-1}\text{s}^{-1}$)	μ_{e} ($10^{-4}\text{cm}^2\text{V}^{-1}\text{s}^{-1}$)	$V_{\text{TFL,h}}$ (V)	$n_{\text{t,h}}$ (10^{15}cm^{-3})	$V_{\text{TFL,e}}$ (V)	$n_{\text{t,e}}$ (10^{16}cm^{-3})
Y6	6.70±0.50	1.72±0.04	0.112	5.80	0.208	1.08
0.5%PCE10:Y6	3.37±0.44	1.78±0.05	0.131	6.78	0.208	1.08
1.0%PCE10:Y6	1.84±0.26	1.83±0.04	0.164	8.50	0.206	1.07

^a The average values were obtained from more than 5 independent devices.

Table S7. The built-in voltage (V_{bi}) and the length of the space-charge region (L_{S}) of Y6-based devices under dark and light (100 mA/cm² sunlight simulator) conditions.

Materials	Condition	V_{bi} (V)	L_{S} (nm)
Y6	dark	0.945	171
	light	0.907	152
0.5%PM6:Y6	dark	0.896	176
	light	0.876	81
1.0%PM6:Y6	dark	0.884	176
	light	0.816	47

Table S8. The excited state energy, hole delocalization index (HDI, a higher HDI means lower hole delocalization), electron delocalization index (EDI, a higher EDI means lower electron delocalization) and integral of Sr function (Sr index, a higher Sr index means a higher spatial overlap between hole and electron wavefunctions) of N4 and Y6 single molecule.

	S_1 (eV)	HDI	EDI	Sr index	Ref
N4	1.821	4.64	4.29	0.667	[4]
Y6	1.832	4.54	4.19	0.659	/

Table S9. PL quenching efficiency (PLQE) of 0.5%PM6:N4 and 1.0%PM6:N4 with exciting wavelengths.

λ_{exc} (nm)	PLQE _{0.5%}	PLQE _{1.0%}	PLQE _{1.0%} / PLQE _{0.5%}
750	0.221	0.341	1.543
700	0.234	0.348	1.487
650	0.230	0.351	1.526
600	0.243	0.363	1.494
550	0.208	0.310	1.490

Table S10. Photovoltaic performance of PM6:N4 devices with various weight ratios. ^a

Ratio	V_{OC} (V)	FF (%)	J_{SC} (mA cm ⁻²)	PCE (%)	J_{SC} (EQE) (mA cm ⁻²)
0:1	0.850 (0.845±0.011)	30.00 (29.39±0.94)	0.46 (0.44±0.01)	0.12 (0.11±0.00)	/
0.005:1	0.865 (0.857±0.010)	37.75 (37.57±0.53)	2.11 (1.88±0.12)	0.69 (0.60±0.05)	2.200
0.01:1	0.865 (0.861±0.006)	43.70 (42.90±0.47)	3.50 (3.31±0.11)	1.32 (1.22±0.04)	3.802

^a The maximum and average values were obtained from more than 10 independent devices.

Table S11. Summary of HOMO level, LUMO level and optical band gap of N4 pure films and blended with various amounts of PM6.

Materials	HOMO (eV)	LUMO (eV)	E_{opt} (eV)
N4	-5.72	-3.86	1.487
0.5%PM6:N4	-5.74	-3.88	1.487
1.0%PM6:N4	-5.74	-3.90	1.487

Table S12. Mobility of N4 blended with various amounts of PM6. ^a

Materials	μ_h ($10^{-4}\text{cm}^2\text{V}^{-1}\text{s}^{-1}$)	μ_e ($10^{-4}\text{cm}^2\text{V}^{-1}\text{s}^{-1}$)
N4	1.57±0.09	1.26±0.04
0.5%PM6:N4	1.52±0.10	1.27±0.04
1.0%PM6:N4	1.47±0.12	1.30±0.02

^a The average values were obtained from more than 5 independent devices.

Table S13. The ratio of μ_h/μ_e , double carrier mobility (μ_{eff}) and Langevin prefactor (γ_{pre}) of N4 blended with various amounts of PM6.

Materials	μ_h/μ_e	μ_{eff} ($10^{-4}\text{cm}^2\text{V}^{-1}\text{s}^{-1}$)	γ_{pre}
N4	1.26	4.36±0.02	1
0.5%PM6:N4	1.20	4.46±0.02	0.897
1.0%PM6:N4	1.13	4.90±0.04	0.653

^a The average values were obtained from more than 5 independent devices.

References

1. A. Hexemer, W. Bras, J. Glossinger, E. Schaible, E. Gann, R. Kirian, A. MacDowell, M. Church, B. Rude and H. Padmore, *J. Phys. Conf. Ser.*, 2010, **247**, 012007.
2. G. F. Burkhard, E. T. Hoke and M. D. McGehee, *Adv. Mater.*, 2010, **22**, 3293-3297.
3. S. Gao, L. Bu, Z. Zheng, X. Wang, W. Wang, L. Zhou, J. Hou and G. Lu, *AIP Adv.*, 2017, **7**, 045312.
4. Y. Tang, Y. Cui, R. Zhang, W. Xue, W. Ma and H. Yan, *Adv. Energy Mater.*, 2024, **14**, 2303799.
5. B. Ray, A. G. Baradwaj, M. R. Khan, B. W. Boudouris and M. A. Alam, *Proc. Natl. Acad. Sci.*, 2015, **112**, 11193-11198.
6. V. V. Brus, C. M. Proctor, N. A. Ran and T. Q. Nguyen, *Adv. Energy Mater.*, 2016, **6**, 1502250.
7. D. Bartesaghi, I. d. C. Pérez, J. Kniepert, S. Roland, M. Turbiez, D. Neher and L. J. A. Koster, *Nat. Commun.*, 2015, **6**, 9929.
8. W. Xue, Z. Zhang, S. K. So, Y. Song, Z. Wei, W. Ma and H. Yan, *ACS Appl. Energy Mater.*, 2022, **5**, 9929-9937.
9. B. Siegmund, M. T. Sajjad, J. Widmer, D. Ray, C. Koerner, M. Riede, K. Leo, I. D. W. Samuel and K. Vandewal, *Adv. Mater.*, 2017, **29**, 1604424.
10. Y. Firdaus, V. M. Le Corre, S. Karuthedath, W. Liu, A. Markina, W. Huang, S. Chattopadhyay, M. M. Nahid, M. I. Nugraha, Y. Lin, A. Seitkhan, A. Basu, W. Zhang, I. McCulloch, H. Ade, J. Labram, F. Laquai, D. Andrienko, L. J. A. Koster and T. D. Anthopoulos, *Nat. Commun.*, 2020, **11**, 5220.
11. Y. Tang, H. Zheng, X. Zhou, Z. Tang, W. Ma and H. Yan, *Energy Environ. Sci.*, 2023, **16**, 653-662.
12. T. Lu and F. Chen, *J. Comput. Chem.*, 2011, **33**, 580-592.
13. Z. Liu, T. Lu and Q. Chen, *Carbon*, 2020, **165**, 461-467.
14. F. Neese, *WIREs Comput. Mol. Sci.*, 2022, **12**, e1606.